Research article

Bruno Romeira*, José M. L. Figueiredo and Julien Javaloyes

NanoLEDs for energy-efficient and gigahertz-speed spike-based sub-λ neuromorphic nanophotonic computing

https://doi.org/10.1515/nanoph-2020-0177
Received March 7, 2020; accepted May 1, 2020; published online June 25, 2020

Abstract: Event-activated biological-inspired subwavelength (sub-λ) photonic neural networks are of key importance for future energy-efficient and high-bandwidth artificial intelligence systems. However, a miniaturized light-emitting nanosource for spike-based operation of interest for neuromorphic optical computing is still lacking. In this work, we propose and theoretically analyze a novel nanoscale nanophotonic neuron circuit. It is formed by a quantum resonant tunneling (QRT) nanostructure monolithic integrated into a sub-λ metal-cavity nanolight-emitting diode (nanoLED). The resulting optical nanosource displays a negative differential conductance which controls the all-or-nothing optical spiking response of the nanoLED. Here we demonstrate efficient activation of the spiking response via high-speed nonlinear electrical modulation of the nanoLED. A model that combines the dynamical equations of the circuit which considers the nonlinear voltage-controlled current characteristic, and rate equations that takes into account the Purcell enhancement of the spontaneous emission, is used to provide a theoretical framework to investigate the optical spiking dynamic properties of the neuromorphic nanoLED. We show inhibitory- and excitatory-like optical spikes at multi-gigahertz speeds can be achieved upon receiving exceptionally low (sub-10 mV) synaptic-like electrical activation signals, lower than biological voltages of 100 mV, and with remarkably low energy consumption, in the range of 10–100 fJ per emitted spike. Importantly, the energy per spike is roughly constant and almost independent of the incoming modulating frequency signal, which is markedly different from conventional current modulation schemes. This method of spike generation in neuromorphic nanoLED devices paves the way for sub-λ incoherent neural elements for fast and efficient asynchronous neural computation in photonic spiking neural networks.

Keywords: nanolight-emitting diodes (nanoLEDs); neuromorphic nanophotonic computing; Purcell effect; quantum resonant tunneling (QRT); spiking neural networks; subwavelength devices.

***Corresponding author: Bruno Romeira**, Ultrafast Bio- and Nanophotonics Group, INL - International Iberian Nanotechnology Laboratory, Av. Mestre José Veiga s/n, 4715-330 Braga, Portugal, E-mail: bruno.romeira@inl.int. https://orcid.org/0000-0002-1485-6665
José M. L. Figueiredo: Centra-Ciências and Departamento de Física, Faculdade de Ciências, Universidade de Lisboa, Campo Grande, 1749-016 Lisboa, Portugal, E-mail: jmfigueiredo@ciencias.ulisboa.pt
Julien Javaloyes: Departament de Física, Universitat de les Illes Balears and Institute of Applied Computing and Community Code (IAC-3), C/ Valldemossa km 7.5, 07122 Mallorca, Spain, E-mail: julien.javaloyes@uib.es

1 Introduction

Artificial intelligence (AI) systems using computing algorithms of deep learning neural networks (DNNs) are emerging rapidly [1]. Despite the truly remarkable achievements of algorithms of neural networks executing intelligent, human-like, tasks such as pattern recognition and decision-making (e. g. AlphaGo [2]), the power budget involved in running these DNNs in standard von Neumann computers is growing exponentially [3]. Instead, the human brain is more than five orders of magnitude more efficient than all current DNNs [4, 5]. The key difference relies in the vast connectivity of the brain that takes advantage of a unique sparse and extremely efficient information transfer via the action potentials in neurons – known as “nerve impulses” or “spikes”.

Currently, AI systems rely on three main generations of neural networks based on their neuronal functionality [6]: i) the McCullock-Pitt perceptron which performs thresholding operation resulting in a digital output; ii) DNN which adds continuous nonlinearity to the neuronal unit enabling to have multiple hidden layers between input and output; and iii) spiking neural network (SNN) that uses neuronal units that exchange information via spikes. SNNs use the timing of the spikes (binary events) to process

information whereas the neuronal unit is only active when receiving or emitting spikes. This reduces substantially the energy over a given period of time. It is estimated that in the brain a consumption of only ~10^4 adenosine triphosphate (ATP) molecules is needed to transmit a spike (bit) at a chemical synapse [7], equivalent to ~1 fJ/bit at 32 bit/s.

Neuromorphic hardware elements for spiking emulation have been addressed using electronics (e. g., TrueNorth using complementary metal-oxide-semiconductors [8]) but typically operate at low speeds (~kHz) and consume several pJ/spike. For low energy, sub-pJ/spike, synaptic-like functionalities, non-volatile materials such as resistive random-access memory, phase-change memory and spin-transfer torque magnetic random-access-memory offer alternatives to silicon (see [9–11] for a comprehensive review). Despite the remarkable progresses, fan-out and parasitic constraints of electronic approaches limit the power budget for scalable solutions.

In the context of photonics, demonstrations of optical neural networks using coherent light-based DNN accelerators [12, 13] and reservoir computing [14, 15], take advantage of the high bandwidth-distance products, lower electromagnetic interference and lower power consumption of optical interconnects [16]. Although these architectures do not use spike-based learning they are capable of remarkable light-based, human-like, recognition tasks under supervised learning [15]. In order reproduce the powerful computation of biological neurons at lower energy cost there has been numerous implementations of spike-based photonic neurons using graphene excitable lasers [17], distributed feedback (DFB) lasers [18], vertical-cavity surface-emitting lasers (VCSEL) [19, 20], time-delayed optoelectronic nanoscale resonators [21], micropillar lasers [22], or phase change materials [23] to name a few (for an extensive review see [24]). Nevertheless, the large footprint (>100 μm^2) of most of these elements is imposing a bottleneck for compact and efficient optical SNNs. A key driver for scalable SNNs is aggressive scaling-down of existing photonic elements, specifically the optical source, to the sub-μm scale for efficient (<10 fJ/spike), fast (>10 GHz) and miniaturized solutions. However, the development of such a subwavelength-scale (sub-λ) light source, well-matched for brain-like photonic spike-based computing, remains a challenge.

In order to reduce the size of a light source well below the micrometer scale, a plethora of nanolasers have been proposed in the last 15 years using photonic crystal cavities [25–27], metallic-cavity cavities [28] and plasmonic cavities [29] (for an extensive review see [30, 31]), but the unlocking of their potential for neuromorphic computing remains unexplored. However, for short distance intra-chip interconnections and brain-like asynchronous neural computation, lasing is not a main requirement turning incoherent nanolight-emitting diode (nanoLED) sources as excellent alternatives to nanolasers. Differently from nanolasers, nanoLEDs do not require a lasing threshold and therefore do not need a high-Q cavity, resulting in much lower current operation requirements [32]. Importantly, in recent years several advances have been made to increase the efficiency of nanoLEDs towards >10% which include Purcell enhancement of radiative emission [33–35], suppression of nonradiative surface effects via chemical passivation treatments [36], and efficient waveguide-coupling methods [37, 38]. NanoLEDs have been already demonstrated for a photonic crystal (PhC) LED [39], a plasmonic LED [40] and a waveguide-coupled nanoLED [37], showing output power levels in the order of tens to hundreds of pW for the PhC case and up to 300 nW for the waveguide-coupled case. Nonetheless, all these reported LEDs are "linear" devices not featuring non-linear spiking-like activation in the form of short pulses, which is crucial to reproduce the biological neural dynamics, as already shown for the case of optically pumped microlasers [22]. To overcome this, a circuit using a neuron-like superconducting-nanowire single-photon detector driving an LED has been proposed for cryogenic neuromorphic computing [41]. However, the low-temperature requirements and slow speed (~MHz) limited by the spontaneous emission rate (~ns), limits this approach for efficient, high-speed and compact solutions.

In this work, we propose and theoretically analyze a novel sub-λ nanophotonic spiking neuron circuit. It is based on a metal-cavity neuromorphic nanoLED for event-driven neural computation. The semiconductor epitaxial heterostructure of our neuron-like unit is formed by a quantum resonant tunneling (QRT) nanostructure monolithic integrated in a double heterostructure LED. The QRT enables control of the injection of electrons into the active region of the LED. This provides an intensity modulated nanoLED with a voltage-controlled negative differential conductance (NDC). The activation of the all-or-nothing optical spiking response (called excitable) is achieved via high-speed nonlinear electrical modulation of the nanoLED. Importantly, the sub-λ metal-cavity offers strong light–matter interaction at the nanoscale via the Purcell effect [30], which scales inversely with the mode volume [31, 38], leading to faster and more efficient light emission and of advantage for high-bandwidth optical spiking. Using a model that combines the dynamical equations of the circuit and rate equations, and using realistic parameters

of a nanodevice that takes into account material parameters, nonradiative effects and size scaling, we analyze the characteristics of the fired optical spikes. We conclude that for optical nanosources with ~0.01 μm^2 mode volume, intensity modulated optical spiking with sub-nanosecond refractory time responses can be achieved upon receiving exceptionally low (sub-10 mV) incoming synaptic-like activation signals, close to the shot-noise limit. This is lower than the amplitude of 100 mV in biological counterparts and much smaller than the typical switching voltages (0.2–2 V) of memristive devices [42]. Notably, we conclude the optical energy per spike is roughly constant and therefore, at some extent, almost independent of the incoming modulating frequency signal, a situation markedly different from standard current modulation methods of light sources [31, 37, 43]. This provides a new modulation scheme in nanoLEDs featuring all the key requirements of spike-based sub-λ neuromorphic optical computing.

2 Key ingredients of neuromorphic nanoLEDs

2.1 Low-dimensional quantum resonant tunneling (QRT) nanostructures

Semiconductor QRT nanostructures use a single or multiple double barrier quantum well (DBQW) of around 10 nm thick in the epitaxial growth direction for 1D carrier confinement and filtering [44]. The energy passband-like filtering leads to a current-voltage (I-V) characteristic displaying a region of NDC that persists at room-temperature from direct current (DC) up to terahertz [44]. These structures when employing a single DBQW are widely known as resonant tunneling diodes (RTDs), and can have cut-off frequencies up to 1.9 THz [45]. Remarkably, the theoretical cut-off frequency of single DBQW-QRTs is limited by the tunneling escape time in the quantum well [44]. As a result, the quantum resonant tunneling effect and NDC characteristic has been exploited in a wide-range of electronic and photonic devices, including THz quantum cascade lasers for gas sensing [46], THz emitters and detectors for imaging [47], and communications beyond 5G (world record oscillation at 1.92 THz [45]), single-photon switches and detectors [48, 49], electroluminescence in III-nitride LED sources [50], III-V unipolar bistable QRT [51], bipolar QRT-based LEDs [52–54] and lasers [55, 56], near-IR photodetectors for optical communications [57], and mid-IR detectors for sensing [58], to name only a few.

For neuron computation, early works evoked QRT-based devices as potential nanoelectronic candidates for cellular neural networks as a form of threshold logical gates [59]. In the context of photonics, early works on n-type (unipolar) QRT nanostructures integrated with highly photo-sensitive absorption layers of interest for synaptic- and autaptic-like bio-neural functionalities have been exploited using either bistable or excitable regimes to enable stochastic resonance [60], spiking [61] or autaptic (self-feedback) neuron-like signaling [21]. Despite these works, the monolithic integration of QRT nanostructures in light-emitting configurations at the nanoscale for ultrafast and energy-efficient spike-based sub-λ neuromorphic functionalities remains unexplored.

2.2 Neuromorphic nanoLED device

The sub-λ nanophotonic spiking neuron unit proposed here is formed by a quantum resonant tunneling (QRT) nanostructure monolithic integrated in a double heterostructure LED, Figure 1A. The LED section consists of an inverted p-i-n AlGAs/GaAs/AlGaAs double heterostructure. The active region is made of GaAs for emission at ~850 nm. Depending on the target emission, alternative active materials can be considered, namely quantum wells or quantum dots. The surrounding layers of AlGaAs (30% Al) with a lower refractive index are included for light confinement in the active region. The QRT section, crucial for the neuromorphic functionality, consists of a nanolayer formed by a lower band gap GaAs material, the well, sandwiched between two thinner layers of a larger bandgap AlAs material, the barriers. The QRT is monolithic integrated in the cathode (n-type region) section of the inverted p-i-n LED, Figure 1A. This minimizes the impact of the QRT on the LED optical performance, as previously considered in the monolithic integration of large area RTD-lasers [55, 56]. This is different from the situation where the QRT is embedded in the active region which shows poor performance at RT mainly attributed to the inefficient resonant tunneling hole injection and other hole current contributions [52, 53]. The QRT enables control of the injection of electrons into the active region of the LED. This provides a nanoLED with voltage-controlled NDC, red solid line in the top panel of Figure 1B, and is markedly different from the “linear” DC current-voltage characteristics of conventional LEDs (black dashed line). As a result, the all-or-nothing spiking (pulse-like) dynamic properties of

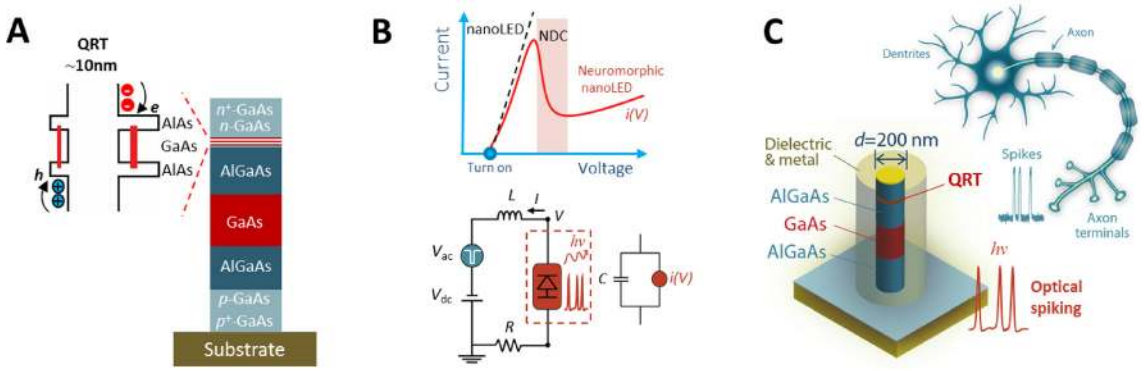

Figure 1: General description of the sub-λ nanophotonic neuron. **A** Schematic of the semiconductor epitaxial heterostructure (not to scale). It is formed by a QRT nanostructure monolithic integrated in a AlGaAs/GaAs/AlGaAs light-emitting diode epitaxial heterostrucuture. In the inset is shown the 10-nm thick QRT AlAs/GaAs/AlAs nanostructure in the $n^+ n n^+$ section. **B** (Top panel) Comparison of the *I-V* curves between a standard nanoLED (dashed line) and a neuromorphic nanoLED (solid red line). The neuromorphic nanoLED features an $i(V)$ with a voltage-controlled NDC. (Lower panel) Schematic of the circuit. The diode is modeled by a nonlinear voltage-controlled current source, $i(V)$, in parallel with the equivalent capacitance, C. The resistance, R, and inductance, L, are the equivalent lumped elements of the LED and electrical connections. The circuit includes a DC voltage source, V_{dc}, and a voltage time-dependent signal, V_{ac}, for synaptic-like activation of the all-or-nothing spiking response. **C** Schematic of the sub-λ nanophotonic neuron in a 200 nm cross section nanopillar using a metal-dielectric configuration. Inset on top is shown the schematic representation of a biological neuron.

neurons can be reproduced, with refractory time responses limited only by the circuit's *RC* constant, lower panel of Figure 1B, where R is the circuit resistance and C is the circuit capacitance. We note despite the small sizes considered here for the cross section of the nanodevices (~200 nm), Figure 1C, one can still assume the energy of the QRT-based nanoLED is quantized only in the direction of the current flow, whereas other quantization effects due to the size of the structure in other directions will be negligible.

Lastly, to achieve a sub-λ nanophotonic neuron with dimensions approaching the sub-100 nm scale, Figure 1C, a nanopillar metallic cavity is considered. Although here we focus our analysis in metallic cavities we note that this configuration could be exploited, in principle, to other cavity configurations such as PhC or plasmonics. In the metal-cavity, the pillar is surrounded by a dielectric cap material (typically made of SiO_2) and then coated with metal (usually Au or Ag). The metal-cavity envisioned for the neuromorphic nanoLED is similar to the one first reported for a waveguide-coupled nanoLED operating at room-temperature [37]. This enables LED devices with a small footprint and light confinement approaching the sub-100 nm scale. Crucial for the firing of fast spikes, the enhancement of the radiative emission in the cavity mode (also known as the Purcell effect [33]) allow us to potentially decrease the refractory time response of the optical spikes down to the 100 ps timescale. As will be discussed, the main challenges are related with the internal efficiency of the LEDs at room-temperature due to nonradiative effects. However, recent work suggests that sub-micrometer nanopillars can achieve exceptional large extraction efficiencies [62], which would strongly benefit the output power of these sources, even in the situation of unavoidable large nonradiative effects.

2.3 Theoretical model

Here, we describe the theoretical model to analyze the operation of the sub-λ neuromorphic nanoLED. It combines the dynamical equations of the circuit, Figure 1B (lower panel) and rate equations that takes into account the Purcell enhancement of the spontaneous emission. In particular, the rate equations model describing the nanoLED follows a similar formalism already introduced in [34]. However, differently from assuming a typical "linear" DC current input driving the LED, in our case the neuromorphic nanoLED is driven by an N-shape nonlinear voltage-controlled current, $i(V)$, top panel of Figure 1B. Firstly, the dynamical equations for the circuit, lower panel of Figure 1B, allow us to obtain the circuit current, I, and voltage, V, as a function of time:

$$\frac{dV}{dt} = \frac{I - i(V)}{C} \tag{1}$$

$$\frac{dI}{dt} = \frac{V_{dc} + V_{ac} - RI - V}{L} \tag{2}$$

The parameters that enter these equations are as follows. The parameter V_{dc} is the circuit bias voltage, R and L

are the equivalent resistance and inductance of the circuit, respectively. The parameter V_{ac} represents the voltage time-dependent activation signal that provides an incoming synaptic-like signal, in the form, for example, of a pulse signal, to trigger the spiking response. As shown in Figure 1B (lower panel), the LED I-V characteristic is modeled by an N-shape nonlinear voltage-controlled current source, $i(V)$, in parallel with the LED equivalent capacitance, C. The parameter $i(V)$ is an analytical function which describes the *I-V* of the neuromorphic nanoLED mainly defined by the current transport in the QRT nanostructure given by [61, 63]:

$$i(V) = A_1 \ln\left[\frac{1+e^{(B_1-C_1+n_1V)q/k_BT}}{1+e^{(B_1-C_1-n_1V)q/k_BT}}\right]\left[\frac{\pi}{2}+\tan^{-1}\left(\frac{C_1-n_1V}{D_1}\right)\right] + H_2\left(e^{n_2qV/k_BT}-1\right) \tag{3}$$

where q is the electron charge, k_B is the Boltzmann constant, and T the temperature of operation (here assumed T = 300 K). In Eq. (3), the first term (with the multiplying parameter A_1) describes the current flow through the most favorable resonant state of the DBQW using the effective mass approximation theory [64]. This describes the first positive differential conductance (PDC) and the NDC regions of the neuromorphic nanoLED. The second term (with the multiplying factor H_2) is the familiar diode *I-V* characteristic and describes the current above the valley region, i.e. the second PDC region. In the top panel of Figure 1B is displayed a representative $i(V)$ curve given by Eq. (3). We note that from the dynamical analysis perspective, simplified versions of Eq. (3) [65, 66] could be employed to model the nonlinear *I-V* characteristic of the neuromorphic nanoLED.

The nanoLED's rate equations for carrier number, N, and photon number, N_{ph}, employed to describe the electrically modulated nanocavity LED is given by:

$$\frac{dN}{dt} = \frac{\eta_i i(V)}{q} - R_{nr} - R_l - R_{sp,cav} \tag{4}$$

$$\frac{dN_{ph}}{dt} = R_{sp,cav} - \frac{N_{ph}}{\tau_p} \tag{5}$$

where η_i the injection efficiency, $R_{nr} = (\upsilon_s A/V_a + C_A n^2)N$ describes the rate of nonradiative recombination, that accounts for the surface recombination (described by the surface velocity, υ_s, and by the surface area of the active region, A), and for Auger recombination, C_A, and where the n is the carrier density such that $n = N/V_a$, and V_a is the volume of the active region. The term $R_{sp,cav}$ describes the spontaneous recombination rate term in a single-mode resonant cavity [67], and R_l describes the radiative decay into all other modes (or leaky modes). The term N_{ph}/τ_p denotes the photon escape rate determined from the cavity Q-factor (where $\tau_p = \lambda_0 Q/2\pi c$ is the photon lifetime and λ_0 is the wavelength in free space).

Assuming inhomogeneous broadening of the electronic states for a bulk emitter, the photon creation rate by spontaneous emission for homogeneously broadening two-level atom in a resonant cavity can be derived from the Fermi's Golden rule [67]:

$$R_{sp,cav} = \frac{\pi}{\hbar\varepsilon_0\varepsilon_{ra}} d_{if}^2 \frac{V_a\omega_{cav}}{V} \int_{\omega_g}^{\infty} \rho_j(\omega_{vc}) L(\omega_{cav}-\omega_{vc}) f_c(1-f_v) d\omega_{vc} \tag{6}$$

We note that Eq. (6) assumes that the emitter spectral width is broader than the single cavity mode spectral width for a cavity centered at the peak emission. This is typically the case for thermally broadened bulk active materials and has been recently extensively analyzed for both nanolasers and nanoLEDs [34, 67]. It is also the case of our neuromorphic nanoLED operating at room-temperature. In Eq. (6), ε_0 is the dielectric permittivity of free space, ε_{ra} is the relative dielectric constant in the active material, d_{if} is the average dipole moment, V is the cavity mode volume close to the physical cavity volume, ω_{cav} is the cavity mode, $\rho_j(\omega_{vc})$ is the joint density of states, $L(\omega_{cav}-\omega_{vc})$ is the homogeneous broadening lineshape, and f_c, f_v are the Fermi distribution functions calculated at the conduction and valence energies, respectively. Since we are operating in the regime of broad emitters (bulk emitter) as compared to the cavity linewidth and we consider the realistic situation of an active material consisting of an atomic ensemble of incoherent (wide) solid state emitters at room-temperature, dynamical effects of the microscopic polarization should not play a role in the dynamic properties of the nanoLEDs analyzed here.

For simplicity of the numerical analysis, the total spontaneous emission in standard textbooks is often approximated by the bimolecular recombination coefficient, B, of the active semiconductor material [68, 69]. In this situation we can approximate the total spontaneous emission as $\gamma(n)Bn^2$, where $\gamma(n)$ is the carrier-dependent emission enhancement factor. The term $R_{sp,cav}$ can now be defined as $\gamma_m(n)Bn^2$, where $\gamma_m(n)$ is the spontaneous emission enhancement which depends, among other factors, on the mode volume describing the modification of the radiative emission rate in the presence of a small cavity. A similar approach has been already shown to describe reasonably well the static properties of nanolasers [28]. Typically, assuming a fixed value of the

radiative emission rate in the leaky modes, this results in a modification of the spontaneous emission factor, β, calculated as $\beta = \gamma_m(n)/\gamma(n)$. The nanoLED section of the theoretical model now reads:

$$\frac{dN}{dt} = \frac{\eta_i i(V)}{q} - \left(\frac{\upsilon_s A}{V_a} + \gamma(n)Bn + C_A n^2\right)N \tag{7}$$

$$\frac{dN_{ph}}{dt} = \gamma_m(n)BnN - \frac{N_{ph}}{\tau_p} \tag{8}$$

For the nanoLEDS and range of parameters analyzed here the bimolecular recombination approximation describes reasonably well the expected static properties of the nanoLEDs predicted by a full model using $R_{sp,cav}$ [34], as in our analysis we consider spontaneous emission enhancement parameters, $\gamma_m(n)$, in the range of values as a result of the reduction of the mode volume predicted by the full model using $R_{sp,cav}$.

In what follows, departing from the dynamical equations of the circuit, (1), (2), the rate-equation model of the nanoLED, (7), (8), and the nonlinear voltage-controlled current source, (3), we examine the various scenarios of operation of neuromorphic micro- and nanoLEDs in terms of efficiency, speed limits and optical spiking dynamic properties and compare their performance with conventional current modulation schemes of micro- and nanoLED sources.

3 Static and spiking dynamics of neuromorphic nanoLEDs

3.1 Static nonlinear characteristics

In this section, our aim is to analyze the static characteristics of metal-cavity pillar-based LED structures, monolithic integrated with a QRT nanostructure, while considering realistic operation at room-temperature. We assume a practical device showing a representative *I-V* curve with similar features as the ones reported for a sub-μm nanocolumn resonant tunneling device (not considering the LED section) [70]. The *I-V* curve given by Eq. (3) is shown in Figure 2 and features a peak current of ~100 μA, a peak-to-valley-current ratio (PVCR) ~4 and an NDC region with a voltage range of about 50 mV. This *I-V* takes in to account the voltage turn-on of the inverted *p-i-n* junction of ~1.5 V obtained from SILVACO simulations of the nanoLED portion of the full device [71]. We note that for the material system analyzed here, *I-V*s with PVCRs up to six at room-temperature could be obtained using improved design of the DBQW structure [72].

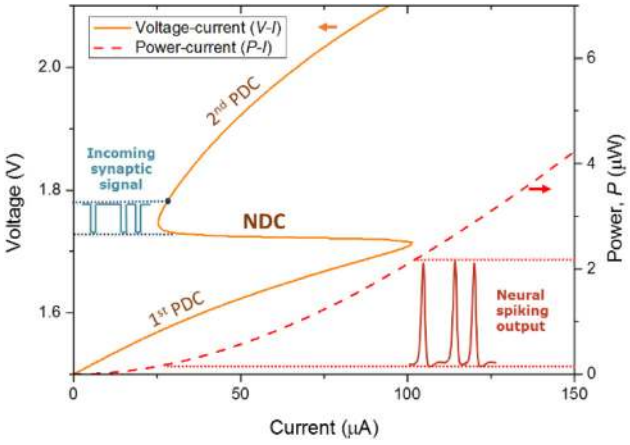

Figure 2: Light-current-voltage characteristics of the neuromorphic nanoLED showing the *V-I* nonlinear voltage-controlled current curve, *i(V)* (yellow solid trace), and the *P-I* curve (red-dashed trace). The *i(V)* with a region of NDC enables voltage induced on-off current switching upon an incoming synaptic-like signal resulting in an all-or-nothing neural spiking output in the optical domain.

For practical analysis and direct comparison we assume two representative neuromorphic LED structures with identical circuit parameters and *I-V* characteristics. The neuromorphic nanoLED is a disk metal-cavity nanopillar with a d = 200 nm cross-section, Figure 1C, where d is the diameter of the semiconductor pillar, and the microLED has a similar disk geometry with d = 2 μm. Since both the microLED and nanoLED rely on the same active material, all the remaining physical parameters were kept constant in both cases (including bimolecular recombination and Auger recombination). We assume a GaAs active material (thickness of 300 nm) using realistic room-temperature bimolecular coefficient, $B = 1.7 \times 10^{-10}$ cm^2 s^{-1}, Auger coefficient, $C = 9.8 \times 10^{-29}$ cm^6 s^{-1}, and surface velocity recombination of 10^5 cm s^{-1}. We assume an effective mode volume scaling keeping a fixed $V_a/V = 0.75$, identical to the nanopillar cavities analyzed in [67]. This corresponds to a mode volume V~0.01 μm^2 for the 200 nm diameter disk nanopillar and a mode volume of V~1.2 μm^2 for the 2 μm diameter micropillar. For these sizes we calculate a value of the spontaneous emission enhancement of γ_m~0.58 for the nanoLED, and of γ_m~0.01 for the microLED at a carrier density of 2×10^{18} cm^3 s^{-1}. For simplicity of analysis, the spontaneous emission enhancement is assumed constant although this value can vary with current injection, as analyzed in [67]. We note this represents the best case scenario of spontaneous emission enhancement and does not take into account non-parabolic bands of the bulk material, or spatial variation of the field in the active region which can further alter the mode volume and reduce the

respective radiative enhancement, particularly in the case of sub-μm devices [67]. However, our goal is not to provide an extensive model that includes all relevant effects but rather an intuitive physical description of practical neuromorphic nanoLEDs with specific focus on their optical spiking dynamic properties. Lastly, we assume for the nanoLED a low-Q factor, $Q = 100$, resulting in a photon lifetime of $\tau_p = 45$ fs, typical of metal-cavities, and assume lower optical losses for the microLED resulting in a photon lifetime of $\tau_p = 450$ fs. In both situations, we use $\lambda_0 = 850$ nm.

For analysis the calculated photon number in (7), (8) is converted to an optical output power using:

$$P = \frac{N_{ph}\eta hc}{\tau_p \lambda_0} \tag{9}$$

where h is Planck's constant, and η the coupling efficiency. For simplicity, both injection and coupling efficiencies were kept constant, and set equal to $\eta_i = \eta = 1$. We note this represents the best case scenario of unity efficiency. Lastly, in our analysis we do not take into account temperature heating effects, which can further reduce the output power, particularly at high injection levels.

Assuming the parameter values described previously, Figure 2 displays the calculated *P-I* curve for the nanoLED device. For current injection levels ~75 μA it displays a power level ~1 μW. In typical electrically current modulated LED sources this corresponds to an optical energy per bit close to 1 fJ at 1 Gb/s. We will use this value as a reference to compare the performance of our LED sources considering that in a practical application the detection of the emission from nanoLED sources requires thermal noise-limited receivers which typically require at least 1 fJ/bit.

Figure 3 displays the calculated *P-V* characteristics showing the optical power versus the injected voltage for the neuromorphic: **A** microLED and **B** nanoLED. The curves were simulated assuming a large value of surface recombination of $\upsilon_s = 10^5$ cm s^{-1}, typical of the GaAs material at room-temperature (solid line), and a low surface value of surface recombination of $\upsilon_s = 10^4$ cm s^{-1}, for the case of improved passivation [73]. In both microLED and nanoLED cases, as the voltage increases from zero, light is emitted as expected after the turn-on of the diode. For a voltage increase up to the $V_{\text{peak}} \sim 1.7$ V, a clear increase of the optical power output is observed as a direct result of the increase of current until a maximum is reached. This current ($I_{\text{peak}} = 104$ μA) is the maximum current in the active region in this voltage range as a result of the tunneling injection of carriers allowed by the QRT nanostructure. In the case of a further increase of the voltage until the valley voltage (V_{valley}), the light output decreases and a pronounced decrease of the emitted power is observed in the region of NDC until the valley current (I_{valley}) is reached. Clearly the optical power follows an N-shape profile which changes nonlinearly with voltage. For the case of the microLED the peak-to-valley-optical-power (PVOP) ratio is 14 at $\upsilon_s = 10^5$ cm s^{-1} and 5.3 at $\upsilon_s = 10^4$ cm s^{-1}, i.e. larger than the PVCR~4 of the *I-V* characteristic, Figure 2. Similar PVOP ratios are obtained in the case of the neuromorphic nanoLED, Figure 3B. The key difference lies in the output power levels achieved. While microLEDs in the current and voltage range analyzed here are limited to power levels well below 1 μW, nanoLEDs show potential to operate >1 μW, specifically when surface recombination can be strongly suppressed. The increased efficiency is directly related to the increase of the spontaneous emission rate in the mode in the case of ultrasmall cavities, and has been extensively analyzed in [34] for the case of InGaAs micro- and nanoLEDs. We note however that reaching power outputs of ~10 μW at RT in practical devices, as shown in Figure 3B, remains an experimental challenge due to Auger recombination and large current density levels which may result in strong heating effects.

In summary, sub-λ neuromorphic LED devices taking advantage of the radiative Purcell enhancement, combined with low surface passivation, can potentially operate at room-temperature with on-chip optical power levels >1 μW (corresponding to ~5000 photons assuming gigahertz per second at the target wavelength), while showing large peak-to-valley-optical-power ratios of advantage for the neuromorphic optical spiking functionality.

3.2 Gigahertz-speed modulation bandwidth

Here, we analyze the modulation bandwidth results for the neuromorphic microLED and nanoLED devices as a function of the voltage-controlled current levels. We analyze the same voltage range as described previously for the case of the static nonlinear characteristics. To obtain the modulation bandwidth, we perform a small-signal analysis of Eqs. (7), (8) with a similar procedure as presented in [69], assuming as input the nonlinear voltage-controlled current curve given by Eq. (3). This allows us to calculate the 3-dB modulation frequency as a function of the voltage, Figure 4. As previously considered, here we investigate the effect of the surface recombination in the modulation speed of the devices. We have excluded from the small-signal analysis the region of NDC since it lies outside the steady-state DC points where other dynamical regimes can occur, namely oscillatory behavior.

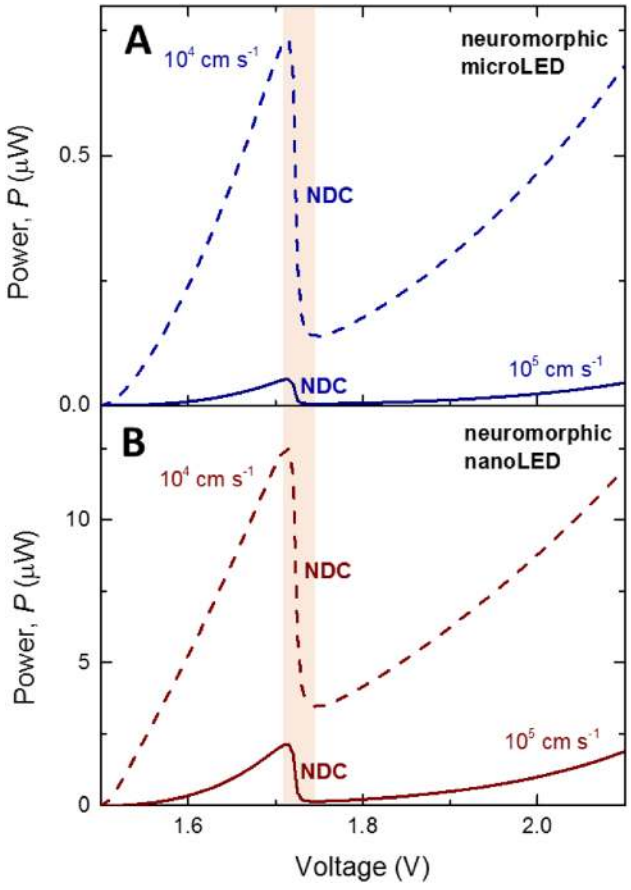

Figure 3: Simulated *P-I* nonlinear characteristics of the neuromorphic **A** microLED, and **B** nanoLED devices. In all curves, the solid lines correspond to a value of surface recombination 10^5 cm s^{-1} and the dashed lines to 10^4 cm s^{-1}. The vertical shadow represents the NDC corresponding to the voltage region where the DC current decreases which leads to a pronounced N-shape characteristic of the emitted optical power.

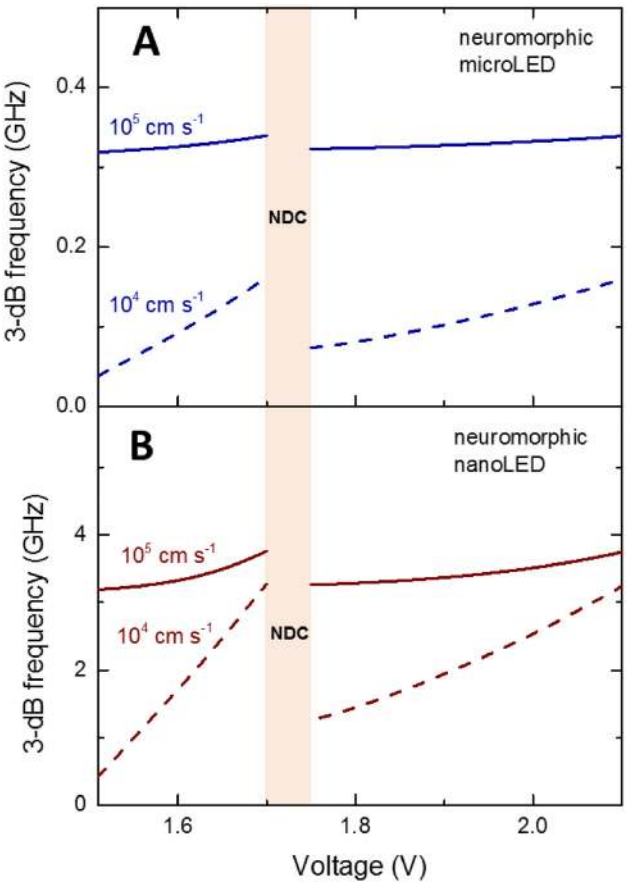

Figure 4: Simulated 3-dB bandwidth versus voltage for the neuromorphic **A** microLED, and **B** nanoLED devices. In all curves, the solid lines correspond to a surface recombination of 10^5 cm s^{-1} and the dashed lines to 10^4 cm s^{-1}. The vertical shadow region represents the NDC corresponding to the voltage region where the DC current decreases.

The simulated curves of the small-signal 3-dB bandwidth versus voltage are shown in Figure 4. In the case of large surface recombination velocity values (solid lines) a maximum modulation bandwidth ~0.34 GHz is achieved for the microLED when operating at the peak voltage ~1.7 V, Figure 4A. In the voltage range analyzed here the modulation bandwidth does not change substantially from its maximum value, even at lower voltage (current) levels. In this case the effect of the surface recombination dominates over the radiative recombination rate. Effectively, this enables to operate the devices faster, even at low current injection levels. In the case of a low surface velocity of 10^4 cm s^{-1} a highly nonlinear 3-dB frequency plot (dashed curves) is obtained. This is as a result of the nonlinear *I-V* input which substantially modifies the current as a function of the applied voltage. In this case, the modulation bandwidth between the peak and valley is reduced from 150 to 70 MHz. This is a result of the reduction of the current injection and consequent lower radiative rate in the case of low surface recombination.

We now analyze the case of the nanoLED, Figure 4B. Assuming a large surface recombination (solid line) a 3-dB frequency of 3.75 GHz can be achieved at the peak voltage ~1.7 V. Assuming the modulation bit rate is 1.3 the 3-dB small signal bandwidth, this corresponds to a modulation bandwidth close to 5 GHz. As described for the microLED, in the case of a low surface recombination (dashed curve) we obtain a highly nonlinear 3-dB frequency plot (dashed curves) due to the nonlinear *I-V* input. In this case, the modulation bandwidth at the peak voltage is ~5 GHz while in the valley region the modulation bandwidth is ~1.7 GHz. Effectively, neuromorphic nanoLEDs benefit from the Purcell enhancement of the radiative emission with potential to support multi-gigahertz speeds for optical spike

modulation. For the nanoLED cases analyzed here, we note that in the peak region the 3-dB variation is not substantial for both low and high-surface recombination cases, while the emitted optical output is well above 1 μW in both scenarios, Figure 3B. Therefore, operating the neuromorphic nanoLEDs in the peak current (where nonradiative channels are already saturated) seems to provide a good compromise between emitted power and speed for both low and large surface recombination values, although as analyzed next the fired spikes would correspond to optical downward spikes.

3.3 Optical spiking dynamic properties

In what follows, departing from the dynamical equations of the circuit, (1), (2), the rate-equation model of the nanoLED, (7), (8), and the nonlinear voltage-controlled current source, (3), we examine the dynamic spike response of the nanoLED via high-speed nonlinear electrical activation. Here we focus our analysis on the activation response for the neuromorphic nanoLED case considering its potential to operate >1 GHz. For this purpose, we assume for the electrical circuit parameters of the nanoLED, lower panel of Figure 1B, an *RC* time constant of τ_{RC} = 310 ps, assuming R = 100 Ω in the best scenario of a low resistance device [74]. The sub-ns *RC* time constant is within the typical modulation bandwidth of the nanoLED analyzed here, see Figure 4B. We note this *RC* time can be realistic achieved in a practical device since it is well above 100 ps, as typically found in state-of-the-art high-speed optoelectronic circuits. Notably, the total dissipated energy of our nanocircuit diode, $E = CV^2$, can be extremely low. As an example, for the case of a 2 μm^2 device resonant tunneling-based microLED device (assuming a 2.8 fF/μm^2 for QRT devices [75] and a 2 V operation), the estimated dissipated energy is ~22 fJ. Lastly, we assume a 3-dB cutoff frequency, f_{3dB}, approximately set by the refractory time, $\tau_{ref} = f_{3dB}^{-1} = 2\pi\sqrt{LC}$ = 440 ps, so that $\tau_{RC} < \tau_{ref}$, i.e. the neuromorphic nanoLED can receive electrically modulated signals at speeds faster than the frequency set by the refractory time. In our circuit, the 3-dB cutoff frequency, $f_{3dB} = 1/2\pi\sqrt{LC}$, is adjusted by the design of the on-chip circuit transmission line, L.

For numerical analysis, we assume the best case scenario of a nanoLED with a low surface recombination and consider operation in a stationary quiescent point for the following DC bias: (a) vicinity of the valley voltage (V = 1.735 V), and (b) vicinity of the peak voltage (V = 1.722 V). In both situations, we assume a synaptic-like weak (sub-10 mV) external electrical stimulus, which forces the bias point out of stable equilibrium. Figure 5A shows the traces of the negative voltage pulses that activate optical upward spikes – excitatory-like signals – and Figure 5C shows the positive voltage pulses that activate optical downward spikes – the inhibitory-like signals. In both scenarios, the shortest incoming stimulus consists of a pulse width of 450 ps (panel (i)), i. e., larger than τ_{RC}. This corresponds to a sub-fJ electrical pulse activation with a value close to the typical shot-noise receivers (~0.13 fJ/bit) [68]. Remarkably, this enables activation of the spiking response using sub-10 mV pulses, Figure 5, which is lower than the amplitude of 50–120 mV in biological counterparts and even much smaller than the typical switching voltages (0.2–2 V) of memristive devices which are promising candidates to emulate biological computing [42]. We note the energy of the incoming stimulus for triggering the all-or-nothing (excitable) spiking response depends on the selected bias quiescent voltage. When the bias approaches the NDC region, the energy required to deterministically fire a spike reduces accordingly, as analyzed in [61, 76].

In the scenario in the valley at V = 1.735 V, panel (i) of Figure 5 A and B, when the input remains below a threshold value, here at –5 mV (dashed red line), the output results in a weak linear response in current that is transformed into a similar quasi-linear optical output, see panel (i) of Figure 5B – this is similar to the standard case of an intensity modulated LED driven by current. When the negative voltage goes above the threshold value of –5 mV, the neuromorphic nanoLED fires a strongly nonlinear response consisting of an optical upward spike – the excitatory-like signal. This is a result of a valley-to-peak current switching induced by the voltage input. An opposite output is achieved in the scenario in the peak at V = 1.735 V, panel (i) of Figure 5C, D. Here the voltage input induces a peak-to-valley current switching resulting in an intensity modulated optical downward spike – the inhibitory-like signal.

We now analyze the remaining properties of the fired upward and downward optical spikes. Provided that the voltage is above the threshold value, the duration in time of the input pulse is less relevant for the characteristics of the output spike. This case is exemplified in panels ii) of Figure 5B, D for three incoming pulses (Figure 5A, C) of 8 mV with a duration of 450 ps, 650 ps and 800 ps. Here, one can appreciate that a longer stimulation leads to an optical spike featuring similar amplitude and full width half maximum (FWHM) of ~320 ps. Lastly, when the duration of the input pulse is larger than the so-called refractory time, multiple optical spikes can be fired. This scenario is displayed in panel iii) of Figure 5B, D showing two optical spikes fired with a time period corresponding to the lethargic time, here ~650 ps. We notice that for realistic

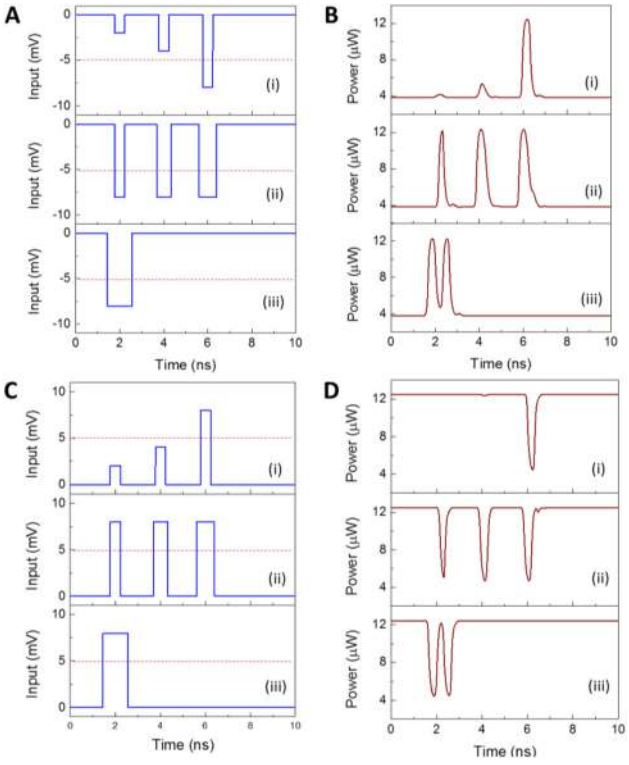

Figure 5: Optical spiking dynamic response of the neuromorphic nanoLED via high-speed nonlinear electrical (sub-10 mV) activation assuming a low surface recombination value. All-or-nothing excitatory (**B**) and inhibitory (**D**) optical spiking responses to incoming synaptic-like negative (**A**) and positive (**B**) voltage activation signals, respectively. The dashed red lines in **A** and **C** indicate the threshold level above which all-or-nothing spiking response is triggered.

operation, the nanoLED excitable spiking response presented here uses incoming pulses of similar duration as the lethargic time of the neuromorphic nanoLED system. A more rigorous definition of all-or-nothing excitable response calls for employing triggering events that are typically much shorter than the lethargic time [77]. In this regard, it is important to mention that our system presents a type II scenario with Fitzhugh-Nagumo-like canard solutions, different from other optical systems, like for example an injected laser, which is a type I via a saddle-node on invariant circle scenario. Independently of the different dynamics involved, an obvious advantage of our neuromorphic nanoLEDs is that lasing is not needed to operate with such spiking responses.

In what follows, we summarize the operation of the neuromorphic nanoLED analyzed in Figure 5D in terms of electrical and optical energy per spike and compare with conventional current modulated (non-spiking) micro- and nanoLED sources. Figure 6 plots the electrical energy as a function of the optical energy per bit for received time duration of the bits ranging from 100 ns to 100 ps. The diagonal lines represent the operation of the LEDs in a non-spiking regime, that is, in a standard current modulation LED scenario operating in the vicinity of the valley voltage, here $V = 1.735$ V. The optical energy is calculated as $P \cdot T$, where T is the bit duration, while for the electrical energy we assume $I \cdot V \cdot T$. In all cases the diagonal curves were only plotted in the regions where the modulation bandwidths are larger than the corresponding bit rate, Figure 4. The dashed lines represent the case of a large surface recombination while the solid lines represent the best case scenario of a low surface recombination. Clearly, the analyzed microLEDs (blue traces) are limited to modulation bandwidths well below 1 GHz and require >100 fJ/bit. Remarkably, nanoLEDs (red traces) are suited for operation in the range 10–100 fJ/bit at multi-gigahertz speed. There is however a compromise between electrical energy and optical energy per bit produced. This is seen in the case of a low surface recombination (red dashed line) where energy consumption close to 10 fJ/bit can be achieved but the optical energies produced are below 1 fJ/bit.

We now analyze the operation of the neuromorphic nanoLED, also operating in the vicinity of the valley voltage. Assuming a scenario of continuous firing of optical spikes so that P is the average optical power output between the peak

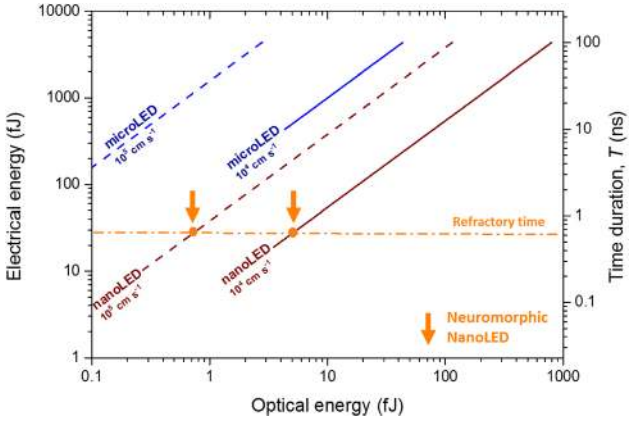

Figure 6: Electrical energy as a function of the optical energy per bit mapped for received time duration of the bits ranging from 100 ns to 100 ps. The diagonal lines are the values for the micro- and nanoLEDs in a non-spiking regime, that is, in a standard current modulation scenario assuming operation in the vicinity of the valley voltage at 1.735 V. The dashed lines represent the case of a large surface recombination of 10^5 cm s^{-1} while the solid lines represent the best case of a low surface recombination, 10^4 cm s^{-1}. The dashed-dot horizontal line is the refractory time of the neuromorphic nanoLED, $\tau_{ref} = 650$ ps. The dashed-dot horizontal orange line intersecting the diagonal traces indicates the refractory time and gives the electrical/optical energy per spike (indicated by the vertical orange arrows) of the neuromorphic nanoLED assuming continuous firing of spikes and operation in the vicinity of the valley voltage.

and valley points of the fired optical spikes, the performance of neuromorphic nanoLED in terms of electrical and optical energy per emitted spike operating in the spiking regime (indicated by the vertical orange arrows in Figure 6), is now set by the intersection between the dashed-dot horizontal orange line (corresponding to the refractory time, τ_{ref} = 650 ps, of the optical nanosource) and the diagonal traces. In this case, the electrical energy per emitted spike is constant ~28 fJ and almost independent of the incoming modulating frequency signal. In the cases of incoming pulses with a time duration larger than the refractory time the energy consumption will increase similarly as already described for a standard nanoLED (diagonal lines in Figure 6). Noteworthy, the optical energy is also almost constant for a given surface recombination value, ~5 fJ for 10^4 cm s^{-1} and ~0.8 fJ for 10^5 cm s^{-1}. Effectively, this allow us to operate the nanoLEDs in the neuromorphic scenario for a large surface recombination at a fixed optical energy close to 1 fJ/spike, and larger than 1 fJ/spike for a lower surface velocity value, and therefore within the range for detection by thermal shot noise-limited receivers. Lastly, we note that in case the device operates in the vicinity of the peak voltage (not shown here), the nanoLED current increases and the corresponding electrical energy per emitted spike increases to ~100 fJ.

In summary, we have analyzed the spiking response of our neuromorphic nanoLEDs via high-speed (sub-ns) nonlinear electrical modulation and have shown low energy consumption in the range of 10–100 fJ upon receiving small amplitude electrical synaptic signals of comparable voltages of biosystems. Although in this work we do not consider the case of incoming optical signals, our approach can potentially provide optically activated neuromorphic nanoLEDs using the photosensitive properties of resonant tunneling structures. Indeed, QRT-based photodetectors have been demonstrated [57, 78] exploiting that the tunneling current is extremely sensitive to changes in the local electrostatic potential, which enables highly-sensitive detection (10^4 A/W) of photogenerated minority charge carriers. Notably, the detection of low-level photons or even of single photons with enhanced quantum-efficiencies above η > 90% can be potentially achieved by integration into photonic cavity structures [79], and this could be explored in future work using our nanocavity LED for fully optically interconnected artificial neurons.

4 Conclusion

In this work, we have analyzed a novel sub-λ nanophotonic spiking neuron circuit suited for spike-based neural computation. The proposed neuromorphic optical nanosource is formed by a quantum resonant tunneling (QRT) nanostructure monolithic integrated into a sub-λ metal-cavity nanoLED. The QRT is a key part of the device enabling control of the injection of electrons into the active region of the LED. This provides an intensity modulated nanoLED with a voltage-controlled negative differential conductance, well suited for all-or-nothing optical spiking modulation. We have examined the various scenarios of operation of two representative neuromorphic micro- and nanoLEDs with realistic operation at room-temperature in terms of efficiency, speed limits and optical spiking dynamic properties, and compared their performance with conventional current modulation schemes of LED sources. We demonstrated inhibitory- and excitatory-like optical spikes at multi-gigahertz speeds can be achieved upon receiving exceptionally low (sub-10 mV) synaptic-like electrical activation signals, lower than the amplitude of 100 mV in biological counterparts and much lower than the typical switching voltages of memristive devices, while providing remarkable low energy consumption, in the range of 10–100 fJ per emitted spike. Importantly, the energy per spike is roughly constant and almost independent of the incoming modulating frequency signal, which is noticeably different from conventional current modulation schemes of LED sources [37, 43]. Although our focus here has been in the analysis of the efficient activation of the optical spiking response via high-speed nonlinear electrical modulation of the nanoLED, this optical nanosource has the potential to enable optical activation of the all-or-nothing spiking response by taking advantage of the highly-sensitive photoresponse of the quantum resonant tunneling nanostructures [48, 57, 60]. Since our nanoLED cavities can be made much smaller than convention optical sources, in a practical application, the electrodes can be as small as the technology for electrical interconnecting to the CMOS chip or even more compact solutions using metal bonding directly to the metal-cavity nanoLEDs. This architecture and method of spike generation in neuromorphic nanoLED devices combined with techniques for more complex interconnectivity (e. g. nanowaveguides [37], or 3D interconnects [80]), paves the way for sub-λ incoherent spiking neural elements for optically interconnected photonic spiking neural networks and asynchronous neural computation.

Acknowledgments: This work was supported in part by the European Commission through the H2020-FET-OPEN

Project "ChipAI" under Grant Agreement 828841. The authors would like to thank Victor Dolores-Calzadilla, Meint Smit and Andrea Fiore, Eindhoven University of Technology, for fruitful discussions on the properties of metallo-dielectric nanoLEDs.

Author contribution: All the authors have accepted responsibility for the entire content of this submitted manuscript and approved submission.

Research funding: This work was supported in part by the European Commission through the H2020-FET-OPEN Project "ChipAI" under Grant Agreement 828841.

Employment or leadership: None declared.

Honorarium: None declared.

Conflict of interest statement: The authors declare no conflicts of interest regarding this article.

References

[1] Y. LeCun, Y. Bengio, and G. Hinton, "Deep learning," *Nature*, vol. 521, no. 7553, pp. 436–444, 2015.

[2] D. Silver, J. Schrittwieser, K. Simonyan, et al., "Mastering the game of go without human knowledge," *Nature*, vol. 550, no. 7676, pp. 354–359, 2017.

[3] X. Xu, Y. Ding, S. X. Hu, et al., "Scaling for edge inference of deep neural networks," *Nat. Electron.*, vol. 1, no. 4, pp. 216–222, 2018.

[4] M. Fischetti, "Computers versus brains," Scientific American, 2011, https://doi.org/10.1038/scientificamerican1111-104.

[5] K. Meier, *The Brain as Computer: Bad at Math, Good at Everything Else*, Salem, MA, IEEE Spectrum, 2017.

[6] S. R. Nandakumar, S. R. Kulkarni, A. V Babu, and B. Rajendran, "Building brain-inspired computing systems: Examining the role of nanoscale devices," *IEEE Nanotechnol. Mag.*, vol. 12, no. 3, pp. 19–35, 2018.

[7] S. B. Laughlin, R. R. de Ruyter van Steveninck, and J. C. Anderson, "The metabolic cost of neural information," *Nat. Neurosci.*, vol. 1, no. 1, pp. 36–41, 1998.

[8] P. A. Merolla, J. V. Arthur, R. Alvarez-Icaza, et al., "A million spiking-neuron integrated circuit with a scalable communication network and interface," *Science*, vol. 345, no. 6197, pp. 668–673, 2014.

[9] D. Ielmini and H.-S. P. Wong, "In-memory computing with resistive switching devices," *Nat. Electron.*, vol. 1, no. 6, pp. 333–343, 2018.

[10] K. Roy, A. Jaiswal, and P. Panda, "Towards spike-based machine intelligence with neuromorphic computing," *Nature*, vol. 575, no. 7784, pp. 607–617, 2019.

[11] J. Zhu, T. Zhang, Y. Yang, and R. Huang, "A comprehensive review on emerging artificial neuromorphic devices," *Appl. Phys. Rev.*, vol. 7, no. 1, p. 11312, 2020.

[12] R. A. Heinz, J. O. Artman, and S. H. Lee, "Matrix multiplication by optical methods," *Appl. Opt.*, vol. 9, no. 9, pp. 2161–2168, Sep. 1970.

[13] Y. Shen, N. C. Harris, S. Skirlo, et al., "Deep learning with coherent nanophotonic circuits," *Nat. Photonics*, vol. 11, no. 7, pp. 441–446, 2017.

[14] D. Brunner, M. C. Soriano, C. R. Mirasso, and I. Fischer, "Parallel photonic information processing at gigabyte per second data rates using transient states," *Nat. Commun.*, vol. 4, no. 1, p. 1364, 2013.

[15] P. Antonik, N. Marsal, D. Brunner, and D. Rontani, "Human action recognition with a large-scale brain-inspired photonic computer," *Nat. Mach. Intell.*, vol. 1, no. 11, pp. 530–537, 2019.

[16] D. A. B. Miller, "Attojoule optoelectronics for low-energy information processing and communications," *J. Light. Technol.*, vol. 35, no. 3, pp. 346–396, Feb. 2017.

[17] B. J. Shastri, M. A. Nahmias, A. N. Tait, A. W. Rodriguez, B. Wu, and P. R. Prucnal, "Spike processing with a graphene excitable laser," *Sci. Rep.*, vol. 6, no. 1, p. 19126, 2016.

[18] H. Peng, G. Angelatos, T. F. de Lima, et al., "Temporal information processing with an integrated laser neuron," *IEEE J. Sel. Top. Quant. Electron.*, vol. 26, no. 1, pp. 1–9, 2020.

[19] T. Deng, J. Robertson, Z. M. Wu, et al., "Stable propagation of inhibited spiking dynamics in vertical-cavity surface-emitting lasers for neuromorphic photonic networks," *IEEE Access*, vol. 6, pp. 67951–67958, 2018.

[20] M. A. Nahmias, B. J. Shastri, A. N. Tait, and P. R. Prucnal, "A leaky integrate-and-fire laser neuron for ultrafast cognitive computing," *IEEE J. Sel. Top. Quant. Electron.*, vol. 19, no. 5, pp. 1–12, 2013.

[21] B. Romeira, R. Avo, J. M. L. Figueiredo, S. Barland, and J. Javaloyes, "Regenerative memory in time-delayed neuromorphic photonic resonators," *Sci. Rep.*, vol. 6, 2016, https://doi.org/10.1038/srep19510.

[22] F. Selmi, R. Braive, G. Beaudoin, et al., "Spike latency and response properties of an excitable micropillar laser," *Phys. Rev. E.*, vol. 94, no. 4, p. 42219, Oct. 2016.

[23] J. Feldmann, N. Youngblood, C. D. Wright, H. Bhaskaran, and W. H. P. Pernice, "All-optical spiking neurosynaptic networks with self-learning capabilities," *Nature*, vol. 569, no. 7755, pp. 208–214, 2019.

[24] P. R. Prucnal, B. J. Shastri, T. F. de Lima, M. A. Nahmias, and A. N. Tait, "Recent progress in semiconductor excitable lasers for photonic spike processing," *Adv. Opt. Photon.*, vol. 8, no. 2, pp. 228–299, Jun. 2016.

[25] B. Ellis, M. Mayer, G. Shambat, et al., "Ultralow-threshold electrically pumped quantum-dot photonic-crystal nanocavity laser," *Nat. Photonics*, vol. 5, p. 297, Apr. 2011.

[26] K. Takeda, T. Sato, A. Shinya, et al., "Few-fJ/bit data transmissions using directly modulated lambda-scale embedded active region photonic-crystal lasers," *Nat. Photonics*, vol. 7, p. 569, May 2013.

[27] G. Crosnier, D. Sanchez, S. Bouchoule, et al., "Hybrid indium phosphide-on-silicon nanolaser diode," *Nat. Photonics*, vol. 11, p. 297, Apr. 2017.

[28] M. T. Hill, Y. Oei, B. Smalbrugge, et al., "Lasing in metallic-coated nanocavities," *Nat. Photonics*, vol. 1, p. 589, Sep. 2007.

[29] R. F. Oulton, V. Sorger, T. Zentgraf, et al., "Plasmon lasers at deep subwavelength scale," *Nature*, vol. 461, p. 629, Aug. 2009.

[30] R. M. Ma and R. F. Oulton, "Applications of nanolasers," *Nat. Nanotechnol.*, vol. 14, no. 1, pp. 12–22, 2019.

[31] M. T. Hill and M. C. Gather, "Advances in small lasers," *Nat. Photonics*, vol. 8, p. 908, Nov. 2014.

[32] K. L. Tsakmakidis, R. W. Boyd, E. Yablonovitch, and X. Zhang, "Large spontaneous-emission enhancements in metallic

nanostructures: towards LEDs faster than lasers \[Invited\]," *Opt. Express*, vol. 24, no. 16, pp. 17916–17927, Aug. 2016.
[33] E. M. Purcell, "Spontaneous emission probabilities at radio frequencies," *Phys. Rev.*, vol. 69, no. 11, p. 681, 1946.
[34] B. Romeira and A. Fiore, "Physical limits of nanoleds and nanolasers for optical communications," *Proc. IEEE*, pp. 1–14, 2019.
[35] M. S. Eggleston, K. Messer, L. Zhang, E. Yablonovitch, and M. C. Wu, "Optical antenna enhanced spontaneous emission," *Proc. Natl. Acad. Sci.*, vol. 112, no. 6, pp. 1704–1709, 2015.
[36] A. Higuera-Rodriguez, B. Romeira, S. Birindelli, et al., "Ultralow surface recombination velocity in passivated InGaAs/InP nanopillars," Nano Lett., vol. 17, no. 4, pp. 2627–2633, Apr. 2017.
[37] V. Dolores-Calzadilla, B. Romeira, F. Pagliano, et al., "Waveguide-coupled nanopillar metal-cavity light-emitting diodes on silicon," *Nat. Commun.*, vol. 8, p. 14323, Feb. 2017.
[38] M. S. Eggleston and M. C. Wu, "Efficient Coupling of an Antenna-Enhanced nanoLED into an Integrated InP Waveguide," *Nano Lett.*, vol. 15, no. 5, pp. 3329–3333, May 2015.
[39] G. Shambat, B. Ellis, A. Majumdar, et al., "Ultrafast direct modulation of a single-mode photonic crystal nanocavity light-emitting diode," *Nat. Commun.*, vol. 2, p. 539, Nov. 2011.
[40] K. C. Y. Huang, M.-K. Seo, T. Sarmiento, Y. Huo, J. S. Harris, and M. L. Brongersma, "Electrically driven subwavelength optical nanocircuits," *Nat. Photonics*, vol. 8, p. 244, Feb. 2014.
[41] J. M. Shainline, S. M. Buckley, R. P. Mirin, and S. W. Nam, "Superconducting optoelectronic circuits for neuromorphic computing," *Phys. Rev. Appl.*, vol. 7, no. 3, p. 34013, Mar. 2017.
[42] T. Fu, X. Liu, H. Gao, et al., "Bioinspired bio-voltage memristors," *Nat. Commun.*, vol. 11, no. 1, p. 1861, 2020.
[43] H. Halbritter, C. Jäger, R. Weber, M. Schwind, and F. Möllmer, "High-speed LED driver for ns-pulse switching of high-current LEDs," *IEEE Photonics Technol. Lett.*, vol. 26, no. 18, pp. 1871–1873, 2014.
[44] C. Ironside, B. Romeira, and J. Figueiredo, *Resonant Tunneling Diode Photonics*, USA, Morgan & Claypool Publishers, 2019.
[45] T. Maekawa, H. Kanaya, S. Suzuki, and M. Asada, "Oscillation up to 1.92 THz in resonant tunneling diode by reduced conduction loss," *Appl. Phys. Express*, vol. 9, no. 2, p. 24101, 2016.
[46] B. S. Williams, "Terahertz quantum-cascade lasers," *Nat. Photonics*, vol. 1, p. 517, Sep. 2007.
[47] T. Miyamoto, A. Yamaguchi, and T. Mukai, "Terahertz imaging system with resonant tunneling diodes," *Jpn. J. Appl. Phys.*, vol. 55, no. 3, p. 32201, 2016.
[48] J. C. Blakesley, P. See, A. J. Shields, et al., "Efficient single photon detection by quantum dot resonant tunneling diodes," *Phys. Rev. Lett.*, vol. 94, no. 6, p. 67401, Feb. 2005.
[49] Q. Weng, Z. An, B. Zhang, et al., "Quantum dot single-photon switches of resonant tunneling current for discriminating-photon-number detection," *Sci. Rep.*, vol. 5, p. 9389, Mar. 2015.
[50] J. Encomendero, V. Protasenko, B. Sensale-Rodriguez, et al., "Broken symmetry effects due to polarization on resonant tunneling transport in double-barrier nitride heterostructures," *Phys. Rev. Appl.*, vol. 11, no. 3, p. 34032, Mar. 2019.
[51] F. Hartmann, A. Pfenning, M. Rebello Sousa Dias, et al., "Temperature tuning from direct to inverted bistable electroluminescence in resonant tunneling diodes," *J. Appl. Phys.*, vol. 122, no. 15, p. 154502, Oct. 2017.
[52] G. Pettinari, N. Balakrishnan, O. Makarovsky, et al., "A micrometer-size movable light emitting area in a resonant tunneling light emitting diode," *Appl. Phys. Lett.*, vol. 103, no. 24, p. 241105, Dec. 2013.
[53] O. Makarovsky, S. Kumar, A. Rastelli, et al., "Direct laser writing of nanoscale light-emitting diodes," *Adv. Mater.*, vol. 22, no. 29, pp. 3176–3180, 2010.
[54] C. Van Hoof, J. Genoe, R. Mertens, G. Borghs, and E. Goovaerts, "Electroluminescence from bipolar resonant tunneling diodes," *Appl. Phys. Lett.*, vol. 60, no. 1, pp. 77–79, Jan. 1992.
[55] T. J. Slight and C. N. Ironside, "Investigation into the integration of a resonant tunnelling diode and an optical communications laser: model and experiment," *IEEE J. Quantum Electron.*, vol. 43, no. 7, pp. 580–587, 2007.
[56] I. Gravé, S. C. Kan, G. Griffel, S. W. Wu, A. Sa'ar, and A. Yariv, "Monolithic integration of a resonant tunneling diode and a quantum well semiconductor laser," *Appl. Phys. Lett.*, vol. 58, no. 2, pp. 110–112, Jan. 1991.
[57] B. Romeira, L. M. Pessoa, H. M. Salgado, C. N. Ironside, and J. M. L. Figueiredo, "Photo-detectors integrated with resonant tunneling diodes," *Sensors (Switzerland)*, vol. 13, no. 7, 2013, https://doi.org/10.3390/s130709464.
[58] F. Rothmayr, A. Pfenning, C. Kistner, et al., "Mid-infrared GaSb-based resonant tunneling diode photodetectors for gas sensing applications," *Appl. Phys. Lett.*, vol. 112, no. 16, p. 161107, Apr. 2018.
[59] M. Hänggi and L. O. Chua, "Cellular neural networks based on resonant tunnelling diodes," *Int. J. Circuit Theory Appl.*, vol. 29, no. 5, pp. 487–504, 2001.
[60] F. Hartmann, L. Gammaitoni, S. Höfling, A. Forchel, and L. Worschech, "Light-induced stochastic resonance in a nanoscale resonant-tunneling diode," *Appl. Phys. Lett.*, vol. 98, no. 24, p. 242109, Jun. 2011.
[61] B. Romeira, J. Javaloyes, C. N. Ironside, J. M. L. Figueiredo, S. Balle, and O. Piro, "Excitability and optical pulse generation in semiconductor lasers driven by resonant tunneling diode photo-detectors," *Opt. Express*, vol. 21, no. 18, pp. 20931–20940, Sep. 2013.
[62] B. Romeira, J. Borme, H. Fonseca, J. Gaspar, and J. B. Nieder, "Strong enhancement of light extraction efficiency in Sub-wavelength AlGaAs/GaAs vertical-emitting nanopillars," in *2019 Conference on Lasers and Electro-Optics Europe and European Quantum Electronics Conference*, Munich, Germany, IEEE, 2019, p. 3–6.
[63] J. N. Schulman, H. J. D. L. Santos, and D. H. Chow, "Physics-based RTD current-voltage equation," *IEEE Electron Device Lett.*, vol. 17, no. 5, pp. 220–222, 1996.
[64] R. Tsu and L. Esaki, "Tunneling in a finite superlattice," *Appl. Phys. Lett.*, vol. 22, no. 11, pp. 562–564, Jun. 1973.
[65] E. R. Brown, W. D. Goodhue, and T. C. L. G. Sollner, "Fundamental oscillations up to 200 GHz in resonant tunneling diodes and new estimates of their maximum oscillation frequency from stationary-state tunneling theory," *J. Appl. Phys.*, vol. 64, no. 3, pp. 1519–1529, 1988.
[66] E. R. Brown, O. B. McMahon, L. J. Mahoney, and K. M. Molvar, "SPICE model of the resonant-tunnelling diode," *Electron. Lett.*, vol. 32, no. 10, pp. 938–940, 1996.

[67] B. Romeira and A. Fiore, "Purcell effect in the stimulated and spontaneous emission rates of nanoscale semiconductor lasers," *IEEE J. Quantum Electron.*, vol. 54, no. 2, 2018.
[68] G. P. Agrawal and N. K. Dutta, *Semiconductor Lasers*, 2nd ed. The Netherlands, Kluwer Academic Publishers Group, 1993.
[69] L. A. Coldren, S. W. Corzine, and M. L. Mashanovitch, *Diode Lasers and Photonic Integrated Circuits*, 2nd ed. Hoboken, NJ, USA, Wiley, 2012.
[70] J. Wensorra, K. M. Indlekofer, M. I. Lepsa, A. Förster, and H. Lüth, "Resonant tunneling in nanocolumns improved by quantum collimation," *Nano Lett.*, vol. 5, no. 12, pp. 2470–2475, Dec. 2005.
[71] Silvaco, *Silvaco ATLAS*, Santa Clara, Silvaco, 2016 [Online]. Available at: www.silvaco.com.
[72] V. K. Reddy, A. J. Tsao, and D. P. Neikirk, "High peak-to-valley current ratio AlGaAs/AlAs/GaAs double barrier resonant tunnelling diodes," *Electron. Lett.*, vol. 26, no. 21, pp. 1742–1744, 1990.
[73] E. Yablonovitch, C. J. Sandroff, R. Bhat, and T. Gmitter, "Nearly ideal electronic properties of sulfide coated GaAs surfaces," *Appl. Phys. Lett.*, vol. 51, no. 6, pp. 439–441, Aug. 1987.
[74] C. Fang, F. Vallini, A. E. Amili, J. S. T. Smalley, and Y. Fainman, "Low resistance tunnel junctions for efficient electrically pumped nanolasers," *IEEE J. Sel. Top. Quant. Electron.*, vol. 23, no. 6, pp. 1–6, 2017.
[75] R. Morariu, J. Wang, A. C. Cornescu, et al., "Accurate small-signal equivalent circuit modeling of resonant tunneling diodes to 110 GHz," *IEEE Trans. Microw. Theory Tech.*, vol. 67, no. 11, pp. 4332–4340, Nov. 2019.
[76] B. Romeira, J. M. L. Figueiredo, and J. Javaloyes, "Delay dynamics of neuromorphic optoelectronic nanoscale resonators: perspectives and applications," *Chaos*, vol. 27, no. 11, 2017.
[77] E. M. Izhikevich, *Dynamical Systems in Neuroscience The Geometry of Excitability and Bursting*, Massachusetts, MIT Press, 2010.
[78] A. Pfenning, F. Hartmann, F. Langer, M. Kamp, S. Höfling, and L. Worschech, "Sensitivity of resonant tunneling diode photodetectors," *Nanotechnology*, vol. 27, no. 35, p. 355202, Jul. 2016.
[79] A. Pfenning, J. Jurkat, A. Naranjo, D. Köck, F. Hartmann, and S. Höfling, "Resonant tunneling diode photon number resolving single-photon detectors," in *Infrared Remote Sensing and Instrumentation XXVII*, United States, International Society for Optics and Photonics, 2019, pp. 47–56.
[80] P. I. Dietrich, M. Blaicher, I. Reuter, et al., "In situ 3D nanoprinting of free-form coupling elements for hybrid photonic integration," *Nat. Photonics*, vol. 12, no. 4, pp. 241–247, 2018.